# Effect of ambient temperature and intracellular pigmentation on photothermal damage rate kinetics

Michael L. Denton
Elharith M. Ahmed
Gary D. Noojin
Amanda J. Tijerina
Giovanna Gamboa
Cherry C. Gonzalez
Benjamin A. Rockwell

SPIE.

# Effect of ambient temperature and intracellular pigmentation on photothermal damage rate kinetics

Michael L. Denton,[a,*] Elharith M. Ahmed,[b] Gary D. Noojin,[b] Amanda J. Tijerina,[c] Giovanna Gamboa,[b] Cherry C. Gonzalez,[a] and Benjamin A. Rockwell[a]
[a]711th Human Performance Wing, Airman Systems Directorate, Bioeffects Division, Optical Radiation Bioeffects Branch, JBSA Fort Sam Houston, Texas, United States
[b]SAIC, JBSA Fort Sam Houston, Texas, United States
[c]Conceptual MindWorks, Inc., JBSA Fort Sam Houston, Texas, United States

**Abstract.** Computational models predicting cell damage responses to transient temperature rises generated by exposure to lasers have implemented the damage integral ($\Omega$), which time integrates the chemical reaction rate constant described by Arrhenius. However, few published reports of empirical temperature histories (thermal profiles) correlated with damage outcomes at the cellular level are available to validate the breadth of applicability of the damage integral. In our study, an analysis of photothermal damage rate processes in cultured retinal pigment epithelium cells indicated good agreement between temperature rise, exposure duration ($\tau$), and threshold cellular damage. Full-frame thermograms recorded at high magnification during laser exposures were overlaid with fluorescence damage images taken 1 h postexposure. From the image overlays, pixels of the thermogram correlated with the boundary of cell death were used to extract threshold thermal profiles. Assessing photothermal responses at these boundaries standardized all data points, irrespective of laser irradiance, damage size, or optical and thermal properties of the cells. These results support the hypothesis that data from boundaries of cell death were equivalent to a minimum visible lesion, where the damage integral approached unity ($\Omega = 1$) at the end of the exposure duration. Empirically resolved Arrhenius coefficients for use in the damage integral determined from exposures at wavelengths of 2 $\mu$m and 532 nm and durations of 0.05–20 s were consistent with literature values. Varying ambient temperature ($T_{amb}$) between 20°C and 40°C during laser exposure did not change the $\tau$-dependent threshold peak temperature ($T_p$). We also show that, although threshold laser irradiance varied due to pigmentation differences, threshold temperatures were irradiance independent. © *The Authors. Published by SPIE under a Creative Commons Attribution 4.0 Unported License. Distribution or reproduction of this work in whole or in part requires full attribution of the original publication, including its DOI.* [DOI: 10.1117/1.JBO.24.6.065002]

Keywords: Arrhenius; photothermal; cells; retinal pigment epithelial; microthermography; kinetics.

Paper 190098R received Apr. 3, 2019; accepted for publication May 30, 2019; published online Jun. 22, 2019.

## 1 Introduction

Innovative applications in industry, medicine, and the military have driven rapid growth in the production of laser systems with novel wavelengths. Too often, the advances have outpaced safety studies for determining safe limits for exposure in humans, which involve lengthy experiments requiring expensive animal models. Without these constraints, nonanimal models[1–3] are useful in the field of laser–tissue interaction. Among these, computational models have gained acceptance in the laser safety community by filling data gaps across laser parameters with predicted laser dose responses.[4–6] Accurate damage projections can also conserve both time and cost by providing rational laser power ranges for use in subsequent animal studies. As an adjunct role to computational models, cell culture models can provide rapid damage response trends relative to varying laser parameters. Additionally, cell culture systems permit flexibility across multiple environmental variables, such as pH, temperature, metabolic states, intracellular pigmentation, and other thermal and optical properties.[6–10] Combined, computational modeling and cell culture (*in vitro*) methods enhance our understanding of laser–tissue interactions resulting from laser exposures across a broad range of environmental, optical, and thermal parameters.

Lasers interact with tissues by mechanisms described as either photomechanical, photochemical, or photothermal.[11] Photothermal damage can be thought of as a multiphasic response in cells. An initial photon absorption and subsequent temperature rise generate thermal transitions in biomolecules, while a delayed metabolic response determines if the cell recovers or dies from the thermal challenge. Living cells use a broad complex set of metabolic pathways and regulatory balances throughout their lifespan.[12] Effects of elevated temperature on these biochemical systems are complex.[13–15] Current understanding of overt thermal damage mechanisms is that cellular proteins denature, aggregate, and lose their biological activity as the result of temperature rise,[13,16] although other macromolecules may be involved at a lower thermal burden.[17] Indeed, using known thermodynamic parameters and calculated denaturation temperatures, Despa's group[17] concluded that a cell's lipid bilayer, and perhaps, some membrane-bound ATPase enzymes are the macromolecules most likely implicated in thermal burn damage. Thus, many biopolymers, especially proteins and lipids, undergo thermal denaturation during mild-to-moderate hyperthermia. The extent of damage to one or more critical protein and/or lipid during this heating phase ultimately determines the fate of the cell.

*Address all correspondence to Michael L. Denton, E-mail: michael.denton.10@us.af.mil

Using a well-controlled experimental system for heating skin to specified temperatures for predetermined time intervals, Henriques and Moritz[18–21] determined that the kinetics of thermal damage was first order. Using the first-order rate law, known as the Arrhenius rate law, the authors established an energy of activation ($E_a$) that was similar to that for denaturation of purified proteins. However, their kinetics model began to weaken at exposure durations ($\tau$) of a few minutes and shorter. More recently, thermal transitions for whole cells and subcellular organelles have been documented using differential scanning calorimetry (DSC).[22–24] Thermal transitions, indicating changes of state of macromolecules (melting/unfolding), identified by DSC also implicate one or more proteins in thermal damage processes, perhaps thermolabile enzymes.

As did Henriques and Moritz, present-day researchers find that short photothermal damage rate processes are not easily determined. In part, this is due to a lack of experimental thermal data that allows a direct comparison between delivered thermal doses with damage outcomes. Fundamental to the Arrhenius rate law is the assumption that the kinetic determinants for damage occur during the heating phase of the photothermal event. While the ability to predict damage based on the expected events occurring during the active heating interval is valuable, understanding biochemical pathways postheating would offer potential modes of intervention. For example, preferential enhancement of photothermal damage to cancerous cells would find medical application, whereas attenuating a damaged pathway could preserve vision after an inadvertent laser exposure at the retina.

In addition to an accumulation of denatured macromolecules, which are the targets for the kinetic approach, regulatory molecules accumulate or diminish in the cellular response to the biochemical chaos produced by thermal doses. In some manner, significant temporal changes in transcription and translation, which ultimately determine cellular fate, result from a fraction of biomolecules that have lost function due to denaturation. There are several known cellular pathways leading to cell mortality[25,26] and the magnitude of the thermal dose is expected to influence the path to death. However, the time of onset for these thermally induced pathways is less clear. Indeed, there are proposed photothermal damage rate process models[27,28] that use a kinetic approach to illustrate how brief heating, via melanin absorption, may lead to a cascade of oxidative chemical reactions that eventually lead to death several hours after laser exposure. Clearly, establishing the induction pathways would aid in identifying key cellular targets for thermal denaturation and thus, refine the kinetic models.

Here, we begin to address the effects of pigmentation, ambient temperature ($T_{amb}$), and laser exposure duration on the damage accumulation rate for photothermal exposure in an RPE cell model optimized for studying threshold temperatures. Our results show a high degree of reproducibility, both with the precision of assigning threshold damage temperatures (experimental) and in the dependence of threshold temperature on laser exposure duration (biological). Our kinetic (Arrhenius) analysis of the thermal data across a broad range of exposure durations indicates a 5%–10% experimental error overall, supporting our view that data from boundaries of cell death are equivalent to a minimum visible lesion, where the damage integral is defined as unity at the end of the exposure duration ($\Omega = 1$ at $\tau$).

## 2 Damage Models

### 2.1 Computational Model

Most damage rate process models are based on the chemical kinetic rate constant most famously associated with the Swedish chemist, Svante Arrhenius. The Arrhenius equation [Eq. (1)] linearly relates the rate ($k$) of an isothermal reaction (production of product $P$) directly to the frequency factor (A; $s^{-1}$) and exponentially to the energy of activation ($E_a$; $J\,mol^{-1}$), temperature ($T$; K), and the universal gas constant ($R$; 8.31 $J\,mol^{-1}\,K^{-1}$).

$$\frac{d[P]}{dt} \propto k = Ae^{\left(-\frac{E_a}{RT}\right)}, \tag{1}$$

$$\Omega(\tau) = A \int_0^\tau e^{-E_a/RT(t')}dt'. \tag{2}$$

When "[P]" is generalized to damage [$D(t)$], then $\frac{dD(t)}{dt} = Ae^{-E_a/RT(t)}$ describes the instantaneous damage rate ($s^{-1}$), and integrating produces $\Omega$, the damage integral [Eq. (2)], which is a measure of accumulated damage. The value of $\Omega$ can be determined at each time step of a thermal profile (temperature versus time). Detailed derivations of $\Omega$ have been provided elsewhere[29–33] and are not presented here. There are other photothermal damage rate process models[27,28] that use a kinetic approach to illustrate how brief heating, via melanin absorption, may lead to a cascade of oxidative chemical reactions that eventually lead to death several hours postlaser exposure. In medicine, where discrete hyperthermic treatments are used in anticancer therapies,[34,35] converting time-at-temperature data to a normalized cumulative number of equivalent minutes at 43°C (CEM 43°C) has proven useful.[13,36,37] In general, this metric is most valuable for long duration hyperthermic treatments and is not assessed here.

The Arrhenius rate parameters $A$ and $E_a$ ($A/E_a$) must be determined empirically. Taking the natural logarithm of the Arrhenius equation [Eq. (1)], linearizes it for the condition of constant (absolute) temperature [Eq. (3)]. Measuring chemical rates at discrete temperatures permits the Arrhenius plot of ln $k$ versus $T^{-1}$, which provides values for $A$ and $E_a$ in the $y$ intercept and slope, respectively:

$$\ln k = \ln A - \left(\frac{E_a}{R}\right)\frac{1}{T}. \tag{3}$$

However, in photothermal damage studies, where the rate of generating a chemical product through thermal conversion cannot be measured in cells, and the reaction is seldom isothermal, a similar linearization is used on the damage integral [Eq. (2)]. When $\Omega = 1$, indicating a level of damage accumulation critical to cells, and integration is carried out over $\tau$, assuming constant peak temperature [$T(t) = T_p$], the linearized form [Eq. (4)] can be rearranged to provide Eq. (5), and a modified Arrhenius plot of ln $\tau$ versus $T_p$ provides values for the Arrhenius rate parameters ($A/E_a$):

$$\ln 1 = \ln A - \left(\frac{E_a}{R}\right)\frac{1}{T_p} + \ln \tau, \tag{4}$$

$$\ln \tau = \left(\frac{E_a}{R}\right)\frac{1}{T_p} - \ln A. \tag{5}$$

Tabulated values of experimentally determined Arrhenius rate coefficients are available[31] for a variety of thermally induced biological transformations, ranging from induction of heat shock proteins[38] to the immediate creation of intracellular bubbles.[39] The tabulated data demonstrate a wide range of values for the coefficients that can be explained, to a limited degree, by the various tissue types and the observational sensitivity for which an effect is determined. For example, retinal lesions are scored differently for damage when an ophthalmoscope is used, as opposed to evaluating histological sections at high magnification. The empirical $E_a$ values listed[31] vary by about one order of magnitude $(200 - 2,000 \text{ kJ mol}^{-1})$, and the frequency factor displays a variance of 254 orders of magnitude. Even with the wide discrepancies in $A$ coefficients, within each empirical dataset $(A/E_a)$, there does exist a logarithmic correlation between the $A/E_a$ values.[30–32] These relationships, shown in Eq. (6)[30] (using kcal mol$^{-1}$) and Eq. (7)[40] (using J mol$^{-1}$), are fit from data derived at the molecular (protein denaturation), cellular, and tissue levels, and include the tabulated data described above.[31] Comparing empirically derived rate coefficients with a line demarked by Eq. (6) or Eq. (7) can provide a useful measure of validity for experimental approaches:

$$\ln A = 1.59E_a - 9.24, \tag{6}$$

$$E_a = 2642 * \ln(A) + 17{,}200. \tag{7}$$

Alternatively, from $\frac{dD(t)}{dt} = Ae^{-E_a/RT(t)}$, one can calculate the critical temperature $(T_{\text{crit}})$ for an experimental system, which mathematically represents the temperature at which $dD(t)/dt = 1$ for the first time during an exposure:

$$T_{\text{crit}} = \frac{E_a}{R \ln A}. \tag{8}$$

As can be shown with Eq. (5), the $T_{\text{crit}}$ equates mathematically to the threshold temperature for a 1-s exposure.[31] The critical temperature value should reflect the type of biological transformation measured and the level of sensitivity provided by the methods chosen. Equation (8) defines $T_{\text{crit}}$ and is calculated by taking the ratio of the slope to the $y$-intercept for data plotted per Eq. (5). Alternatively, the critical temperature can be calculated from any set of $A/E_a$ pairs reported in the literature. For example, the $T_{\text{crit}}$ for the photothermal induction of heat shock proteins in cultured cells[38] is low (48°C) relative to photocoagulation in the retina[41,42] (57.6°C–59.7°C) and whitening of egg albumin using water bath heating[43] (76°C).

## 2.2 Biological Model

Successful *in vitro* models retain phenotypic characteristics and respond to external stimuli in a manner common to cells in the source organ. Cells of the retinal pigment epithelial (RPE) layer contain melanosome particles (MPs), which are highly absorptive to visible light and are the reason the RPE layer is the principal target for photothermal damage in the retina. Unfortunately, RPE cells taken from adult animals have lost their ability to produce endogenous MPs, and in extended culture, the MPs are diluted with each cell division. Our studies with the hTERT-RPE1 cell line show that they retain their

phagocytic functions and can be artificially pigmented.[8–10] Additionally, this artificially pigmented RPE model[8] exhibits damage trends similar to those in nonhuman primates.[44,45]

Well-crafted comparative experiments provide trends in damage sensitivity. Unfortunately, differences in optical and thermal properties between the cell culture model and intact retina make comparing damage thresholds based on laser dose difficult. After photon absorption, and the subsequent temperature rise, the processes of cellular damage likely ensue the same as heat transfer induced without photons, unless there is a subsequent chemical reaction(s) based on the concentration of melanin pigment.[27,28] Therefore, a method that follows the damage rate processes relative to temperature rise, rather than laser dose, avoids complications from varying absorption and diffusivity in samples, regardless of wavelength. Without the inconsistencies of absorptivity and diffusivity of samples, temperature-based damage thresholds will be more comparable across inhomogeneous samples. It is interesting to consider if, based on a fundamental photophysical response rather than laser dosimetry, a thermal damage threshold could be similar in all cell types.

Regardless of the subtleties of cell type, there is the issue of how to assign the thermal threshold. Following typical convention, identifying the temperature rise at the center of a laser exposure site leading to a minimum lesion defines the threshold temperature, regardless of laser irradiance. However, if laser irradiance is too great, the lesion size becomes larger than the minimum, and the central temperature is greater than the threshold. To determine temperature thresholds, one must use large sampling numbers to attempt to get the perfect minimum lesion scenario. This method leads to the discarding of many data points when exposures lead to either no damage or lesions that are too large.

One solution is to use thermal methods that provide data with spatial resolution, which correlate to damage, which is likewise spatially resolved. There are few reports of empirical laser damage studies that combine the two methods. Welch and Polhamus[41] used carefully placed microthermocouples in animal eyes, and Simanovskii et al.[46] spatially modeled the thermal distribution about a centrally measured temperature rise for comparison with fluorescence damage images. Our group has directly measured spatially resolved thermal maps using infrared cameras at high magnification (c.a. $8 \times 8\ \mu$m effective pixels) and high speed (800 fps) for correlation with fluorescence damage images,[47–49] which has been termed microthermography. In essence, these methods provide an estimate of temperature history at the boundary between cells surviving the laser exposure and those that go on to die.

The prime advantage of determining threshold temperature at the boundary of cell death is that the method does not depend upon laser dose. Central temperatures do rise with increasing laser irradiance, whereas the temperature at the boundary of cell death should remain relatively stable because spatially, it represents the biological threshold regardless of the size of damaged tissue (Fig. 1).[47] Also, one can achieve a much greater experimental efficiency using damage boundary data because all exposures resulting in damage, smaller than the laser footprint, are part of the dataset, not just those that produce a minimal lesion.

Temperature history collected at the boundary of cell death is well suited to study the kinetics of cell death. Our hypothesis is that the boundary regions represent the same damage rate processes, not only within the same damage event (perimeter of a
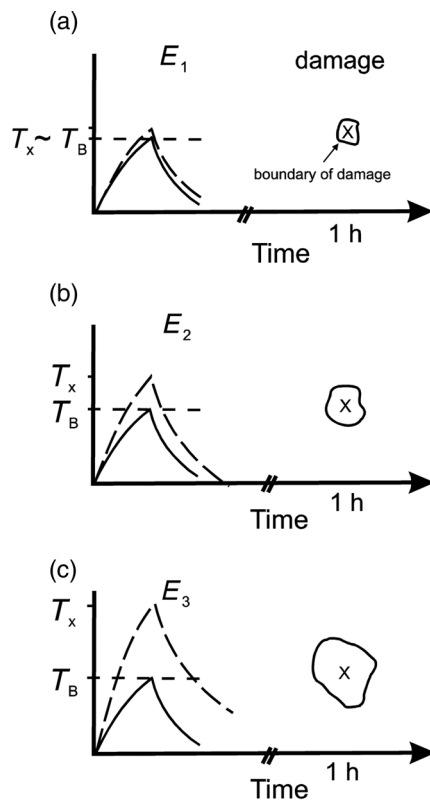
**Fig. 1** Definition of threshold temperature at the boundary of cell death in response to photothermal damage mechanisms. Artificial data are shown to illustrate the relationship between temperature at the center of a laser irradiated region (demarked as an X) and the temperature at the boundary of cell death (arrow). (a) Near-threshold irradiance yields a small area of damage 1-h postexposure and the temperature at the boundary ($T_B$) is only slightly lower than that produced at the center of the exposure site ($T_X$). (b), (c) As laser irradiance is increased above threshold ($E_1 < E_2 < E_3$), $T_X$ rises due to increased absorption. However, $T_B$ remains constant in all exposures because it corresponds to the true biological threshold temperature. Reproduced with permission from Ref. [47].

damaged region) but also for all boundaries of death generated for a given sample and environment. Being identical in damage rate processes, we can, therefore, assign the same damage accumulation, such as $\Omega = 1$. This simple point provides the basis for comparing how changing laser parameters, ambient temperature, and the optical and thermal properties of the tissue effect damage rate processes, if at all.

## 3 Materials and Methods

### 3.1 Cell Culture and Laser Exposure

#### 3.1.1 Pigmented cells (532-nm exposures)

The *in vitro* retinal model employed in this study was developed previously.[8] RPE cells immortalized with hTERT (hTERT RPE-1, ATCC, CRL-4000) were seeded into 24-well glass-bottom (No. 0) tissue culture plates (MatTek, P24G-0-13-F) at $7.0 \times 10^4$ cells/well in DMEM/F-12 media (Cellgro, 15-090-CM), excluding well A1 for monitoring temperature during exposures. After about a day, each well was observed for optimal cell health and confluency (50%–60%). For cultures meeting optimal conditions, MPs were added based on expected cell density at the time of laser exposure (two population doublings

postseed would yield $2.8 \times 10^5$ cells/well). Stock solutions of extracellular MPs from a bovine source were obtained by the isolation method of Dontsov et al.[50] To achieve target pigmentations greater than 200 MPs/cell, multiple additions of 200–250 MPs/cell aliquots (in 0.5 mL complete medium) were added to wells 1.5–2 h apart. Upon completion of MP additions, fresh medium was added to wells to a final volume of 2.0 mL. Cells were then incubated at 37°C, 5% $CO_2$ atmosphere overnight to allow for phagocytosis of MPs. Adhering to this schedule provided monolayers with consistent cell density and good overall viability. In preparation for laser exposures on the second day postseed, wells with optimal MP uptake and overall health (manual inspection of each well) were carefully washed twice with 0.5 mL Hank's balanced salt solution (HBSS) with 10 mM HEPES at pH 7.4 and without sodium bicarbonate (Corning 20-023-CV) (collectively called the exposure buffer) at room temperature. A final rinse with prewarmed exposure buffer in a glove box incubator (37°C) was performed near the exposure box. Wells then received 0.5-mL prewarmed exposure buffer and equilibrated in the exposure chamber (35°C ± 1°C) for at least 10 min before laser exposures.

Laser delivery for exposures of cells with varying pigmentation (100, 200, 400, 800 MPs/cell) is depicted in Fig. 2. As described previously,[49,51] two lenses (L5 and L6) and a fiber coupler were used to launch the 532-nm beam into a 100-$\mu$m core multimode fiber (NA 0.22) and the output of the fiber tip was relay-imaged (1.25× magnification) to the sample plane as a nominal flat top 480 ± 5-$\mu$m diameter image using L3 and L1. Beam diameter was verified using a CCD camera at the sample plane and Spiricon software. In addition to the delivery of the laser, the microscope served to image (L4 and L1) and record video (60 fps) of cell samples, and image (L2 and L1) and record microthermography. A Plexiglas enclosure chamber[49,51–53] provided consistent ambient temperature and 60%–75% relative humidity. As measured by microthermography, the average ambient temperature for all 91 individual 1-s and 3-s exposures was 34.3°C ± 0.3°C. Immediately prior to the automated process at each well, cells at the sample plane were brought into focus with a z-micrometer using the video camera. Imaging cells through glass bottom cell culture dishes eliminated steps for complex liquid handling prior to microthermography that were needed previously.[47] Once exposures were completed, wells in the plates were assessed for cytotoxicity as described below.

#### 3.1.2 Cells without pigment (2-$\mu$m exposures)

We used the same hTERT-RPE1 cell line for laser exposures at 2 $\mu$m without the addition of MPs. Cells (100,000) were seeded (1.0 mL total) into sterile AttoFluor chambers (Molecular Probes) containing 25-mm diameter No. 0 borosilicate coverslip bottoms (Deutsch Deckglaser, Cat. GC-25-0-oz). Up to six AttoFluor chambers were prepared together for laser exposures. On the following day, after cells were carefully washed twice with 1.0-mL exposure buffer, 1.0-mL exposure buffer was added and the chambers were transferred to a 37°C culture incubator (no $CO_2$) adjacent to the exposure bench until each was exposed separately. A custom LabVIEW program automated all imaging and laser delivery processes. Immediately after receiving three replicate exposures (1 mm apart) of a given laser energy at a given ambient temperature, the chambers were placed back into the incubator. Once all six (or fewer) chambers received replicate exposures, the chambers were assessed for cytotoxicity 1 h later, as described below. Using this method,
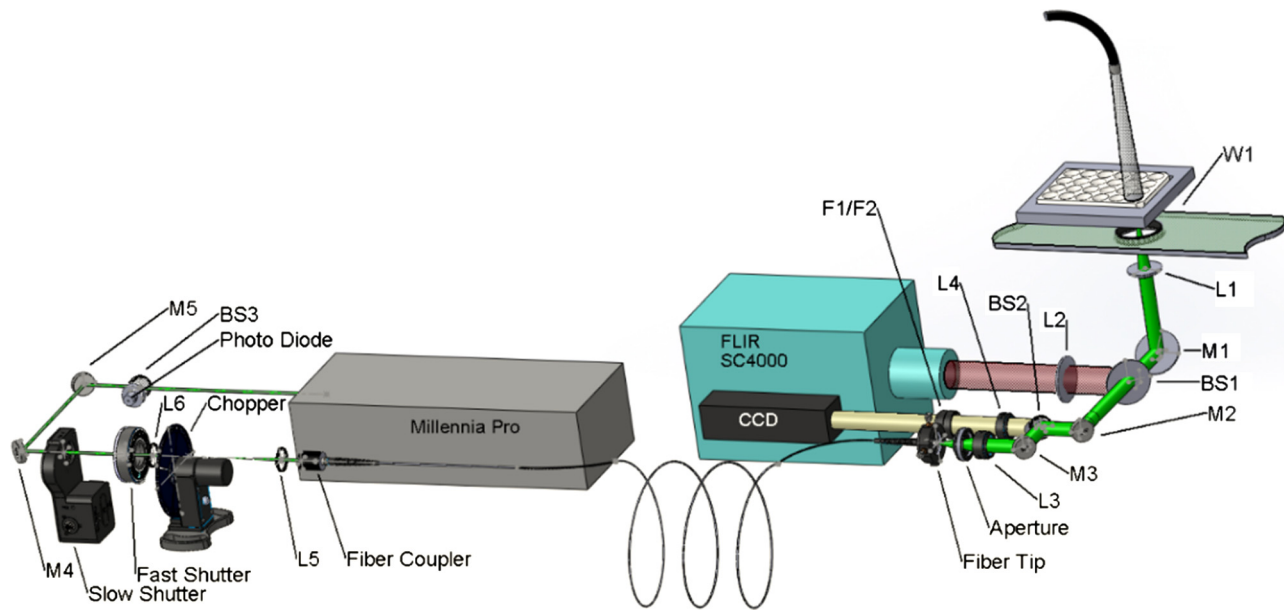
**Fig. 2** Laser delivery to pigmented RPE cells. Output of a 10-W Millennia Pro laser (Spectra Physics, Mountain View, California) was launched into a 100-$\mu$m core multimode fiber. BS3 provided real-time monitoring of laser power. Output from fiber was imaged through the microscope to the wells inside the warmed enclosure. Thermal (FLIR) and video (CCD) imaging utilized beam splitters (BS) 1 and 2. M, mirror; L, lens; W, optical window, F, laser rejection filter (OG570).

the cells were only at the given ambient temperature for the short time needed to achieve the desired temperature and carry out the laser exposures.

A Nikon TE300 microscope stage plate (Linkam part L-PE100/NI, distributed by McCrone Microscopes, Westmont, Illinois) with thermoelectric heating/cooling ($10°C/\min$) was used to obtain various ambient temperatures ($20°C$, $25°C$, $30°C$, and $40°C$) of cells in AttoFluor chambers prior to laser exposure. Preliminarily, cells held at each of the ambient temperatures for an excessive time (15 min) relative to that required to perform exposures (2–5 min) showed no loss in viability as determined by the method used after laser exposure (data not shown). To provide feedback for thermal camera offset

(Sec. 3.3), temperatures of samples were estimated with a micro-thermistor (EPCOS, Cat. B57540G1103F000) held off center and near the surface of the cells via a custom Teflon lid. A heated Plexiglas enclosure similar to that used for the pigmented cell exposures was used to reduce the time needed to achieve the ambient temperatures of $30°C$ and $40°C$.

Both laser delivery and microthermography were carried out from beneath the cells in a similar manner to that described,[53] where the final imaging optic prior to cell samples was a 75-mm $CaF_2$ lens (CF-PX-38-75, ISP Optics, Corp., Irvington, New York). Figure 3 provides a schematic of the experimental set up for the variable ambient temperature experiment. The output of a thulium fiber laser (IPG Photonics, TLR-20-2000-LP)
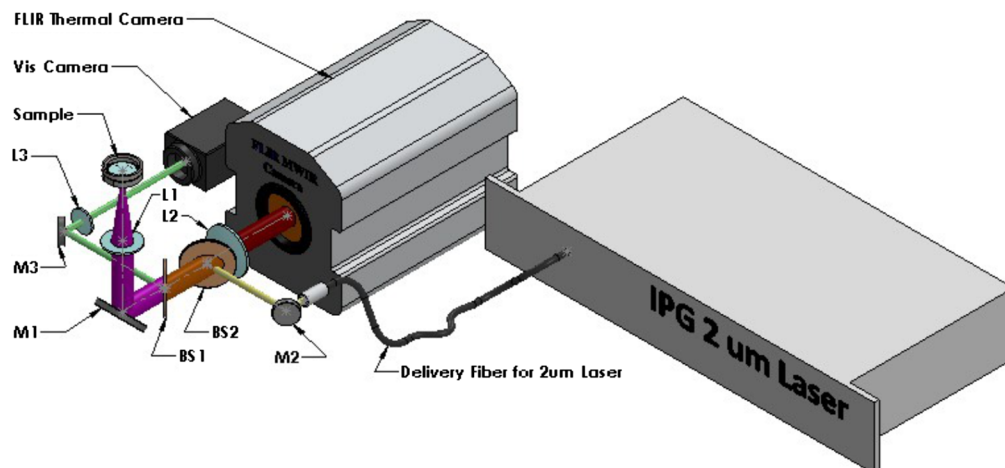


**Fig. 3** Laser delivery to RPE cells without pigment. Output of an IPG Photonics TLR-20-2000-LP fiber laser was delivered to RPE cells (sample) from below. Cells were imaged from below using bright field (PULNiX TM-6701 AN Camera) and microthermography (FLIR thermal camera). Mirror 1 (M1) and lens 1 (L1) were common to both legs of the microscope. Exposures were carried out in a Plexiglas enclosure, which was only closed with heat control for exposures at $T_{amb}$ of $30°C$ and $40°C$.

provided 2-$\mu$m irradiation focused to an approximately Gaussian beam with a diameter of $620 \pm 7$ $\mu$m. The internal laser shutter was computer controlled to deliver exposure durations of 0.05, 0.25, 1.0, and 20 s.

## 3.2 Damage Assessment

Cell death was determined by postlaser exposure in the same manner for all sample types. After exposures, the exposure buffer was replaced with complete medium and cells were incubated at 37°C and 5% $CO_2$ for at least 1 h to allow recovery or damage progression. After recovery, cells were stained for 15 min at 37°C for viability using 1.7-$\mu$M calcein-AM (C3100MP, Life Technologies, Grand Island, New York) and 1.4-$\mu$M ethidium homodimer 1 (EthD1, E3599, Life Technologies) in complete HBSS. Laser-damaged sites were identified by 10× imaging on an Olympus CK-40 using EthD1 channel (bandpass exciter of 475–545 nm and a barrier filter at 590 nm) and Calcein-AM channel (bandpass exciter of 460–490 nm and a bandpass emitter of 490–530 nm). Monochrome images were taken using a Hamamatsu ORCA 100 camera.

Damage threshold irradiance values ($ED_{50}$) were determined using the Probit[54,55] method, as previously described.[8–10] The Probit output included 95% confidence intervals [fiducial limits (FLs)] related to the $ED_{50}$ value. Probit slope values were determined by taking the first derivative of the Probit probability curve at the 50% value.

## 3.3 Microthermography

A ThermoVision SC4000 (532-nm exposures) or SC6000 (2-$\mu$m exposures) mid-wave infrared camera (FLIR Systems, Inc. Boston, Massachusetts) imaged cells at 800 fps during laser exposure. Effective pixel pitch values were 8.61 and 7.41 $\mu$m/pixel for the SC4000 and SC6000, respectively. Knowing that our thermal imaging system involves transmission through thin borosilicate coverslips (no. 0, 0.08–0.12 mm), we characterized the transmission of a clean no. 1 coverslip (average thickness of 0.15 mm) by placing it in front of a blackbody reference source (M316, Mikron Instruments). We found 86% transmittance at the wavelength range specific to the InSb camera detector ($3 - 5$ $\mu$m). During each calibration of the thermal camera, we placed a piece of MatTek well-bottom No. 0 glass (a window) in front of a portable blackbody source (M316, Mikron Instruments). This then accounted for the true transmission of heat by the cells through the bottom of the wells during experiments. After the final optical configuration was established, the nonuniformity correction and the calibration of both the camera and overall thermal imaging system were performed, as suggested by FLIR systems. Specifically, we used reference plates provided by FLIR at two temperatures, different by at least 10°C, and recorded short movies for comparisons of defined RoIs. The calibration was verified by applying the calibration in the ExaminIR software and imaging the black body with the window in place. At several points across the calibration range, the temperature of the black body was compared to the temperature measured by the thermal camera. Our calibration was correct to within 1°C.

Due to the relatively high magnification and speed of our microthermography imaging, coupled with low spectral irradiance for the range of the thermal camera ($3 - 5$ $\mu$m) at around room temperature, there was a minor drift in the camera's offset over time. We devised methods to adjust the thermal camera's digital offset to a known temperature immediately prior to each laser exposure at the two experimental systems. For the pigmented cell exposures, a small cylindrical piece of aluminum was fit snugly into well A1, which effectively placed a coverslip between the camera (SC4000) and the aluminum. The painted (flat black) aluminum was fitted with a resistance temperature detector (RTD) directly into the top. When the $x$, $y$ translational stage was in the "home" position (well A1 centered over the microscope) between laser exposures, we could adjust the thermal camera offset to the temperature verified by the RTD. For the 2-$\mu$m exposures, the real-time temperature feedback from a microthermistor placed just above the cells was used to adjust the thermal camera (SC6000) offset, as also described in Sec. 3.1.2.

## 3.4 Thermal Data Analysis

Thermal data were processed as previously described,[47] with the primary goal of identifying temperatures correlated spatially to the boundary of cell death, which identifies those cells receiving the lowest dose to produce cell death ($\Omega = 1$). Thermal images were used to extract and calculate thermal data from full-frames ($192 \times 192$ pixels) and the boundary of cell death regions of interest (RoIs). After the overlay of thermal and damage images, with proper orientation and stretching protocols, boundary RoI mask files were output. Boundary RoI masks were then used to extract temperatures for pixels corresponding to the boundary of cell death from original FLIR files. Mean thermal profiles for individual exposures were averaged with others within a data ($\tau$) set, and the final mean thermal profiles were reported with both standard deviation (SD) and standard error of the mean (SEM).

## 4 Results and Discussion

When our group began studying photothermal damage processes, we used laser dosimetry to describe threshold damage.[8–10] Due to variations in both absorptivity and diffusivity of our samples, which dictate the rate of temperature rise and cooling, threshold laser irradiance values also varied from sample to sample. In addition, laboratory ambient temperature created a variance in thresholds, and we implemented the use of environmental enclosures with stable temperature and humidity control.[10] Subsequently,[47–49] we decoupled damage relative to laser dosimetry by following temperature rise during laser exposure. In a previous article,[47] we examined the concept that cells at the boundary of cell death, as identified by fluorescent indicator dyes, will have received the minimum temperature history needed for a damaging outcome (Fig. 1). We described methods for overlaying thermal movies, recorded in real time with laser exposure at high speed and high magnification, with corresponding fluorescence damage images such that threshold thermal profiles were obtained. One conclusion from these prior data, which were collected over a fairly narrow range of exposure durations (0.1–1.0 s), was that the threshold peak temperature values were not significantly different from each other. Although the methods for image overlay remain essentially the same, in an effort to challenge the above conclusion, we improved laser delivery and thermal imaging methods, and we now expand the exposure time range to 0.05–20 s.

We continue to consider temperature history at the boundary of cell death a definitive metric for determining the onset of cell death (Fig. 1). Therefore, by design, direct comparisons of

threshold temperatures ($\Omega = 1$ at $\tau$) across the laser exposure durations are expected to be valid, as long as the damage assessment (types of dyes and recovery time) is performed the same way each time. However, the current study is meant to go beyond a simple analysis of thermal profiles and threshold peak temperature values for a variety of laser exposure times. We expand our analyses to include effects of ambient temperature during laser exposure, different chromophores (bulk heating of water versus melanin absorption), and for samples differing only in absorption coefficient (number of MPs). Finally, to assess how well a single empirically determined $A/E_a$ pair predict cell death, we want to use the threshold thermal profiles from the boundary of cell death to compute damage integral values.

## 4.1 Effects of Ambient Temperature on Damage

### 4.1.1 Thermal profiles at the boundary of cell death

Figure 4 depicts steps during the method of extracting thermal data from the boundary of cell death for two representative 2-$\mu$m laser exposures of hTERT-RPE1 cells without pigment. The fluorescence damage images (panels 4b and 4h) show clear demarcation for laser damage and high cell viability outside the damaged regions. The orientation of the damage maps (panels 4c and 4i) relative to the damage images (panels 4b and 4h) reflect multiple flip/rotate functions required for correct overlay (shown) with thermal images (panels 4d and 4j). The resulting overlay of thermal and damage images provided thermal single-pixel RoI maps (panels 4e and 4k) corresponding to the perimeter of the damage map. Mean thermal profiles were derived
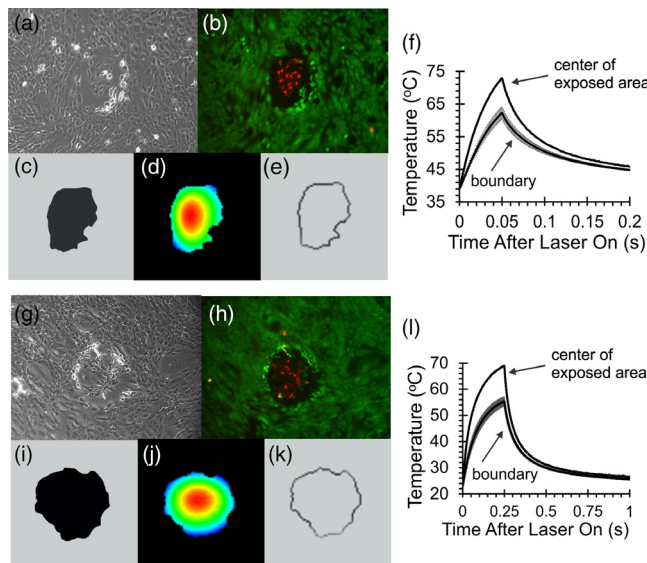


**Fig. 4** Determining threshold thermal profiles at the boundary of cell death. Shown are images representing various stages of extracting thermal data at the boundary of cell death for exposures to 2-$\mu$m laser irradiation for (a)–(f) 50 ms and (g)–(l) 250 ms. (a), (g) Phase contrast images postlaser exposure. (b), (h) Overlaid fluorescence images (calcein and ethidium homodimer) identifying damage. (c), (i) Damage masks generated from calcein images. (d), (j) Thermal maps of corresponding thermograms at the end of laser exposure. (e), (k) Thermal image mask of pixels at the boundary of cell death. (f), (l) Thermal profiles for the 50- and 250-ms laser exposures. The upper profile in each represents the central temperature of (d) and (j) the example exposure; the lower profiles used the mean $\pm$ SEM threshold temperature values for all similar exposure durations.

from averaging the RoI pixels from the original thermal movie of the laser exposure (panels 4f and 4l). Thermal profiles are shown at the boundary (lower-temperature rise profiles with SDs), which can be compared to temperatures at the center of the exposed region (upper-temperature rise profiles).

As an example of constant sample thermal and optical properties, the nonpigmented RPE cells were exposed at 2-$\mu$m for 0.05, 0.25, 1.0, and 20 s. Each set of the four exposure durations was performed at four different ambient temperatures (20°C, 25°C, 30°C, and 40°C). The large number of equivalent pixels (1100-3–207) associated with the 12–20 replicates within each of the 16 types of exposures validated the use of SEM values (Table 1). However, even though the small SEM values indicated the threshold $T_p$ values were statistically significant, they were smaller than the accuracy of the FLIR camera (1°C), and we will refer to SD values because they realistically convey experimental uncertainties.

The $T_{amb} \pm$ SD values in Table 1 provide the support that we achieved the target ambient temperature prior to laser exposure with precision. Again, it took only 2–5 min to reach these ambient temperatures and another 20–90 s to perform the exposures. Beyond this limited time at nonoptimal temperatures, cells either recovered or underwent damage progression at the optimal temperature (37°C). Laser energies were chosen to produce damage, with slight variations leading to damage regions of various sizes. Damaged regions that were nearly the area of the laser, and larger, were avoided in our analysis because they do not accurately represent energy deposition by the laser.

Mean temperature rise ($\Delta T$) profiles, constructed by averaging temperature among replicates at each time point of the thermal movie, are given in Fig. 5. To provide separation between the shorter thermal profiles, Figs. 5(a)–5(d) truncate the 20-s data at 2 s. The diffusivity in our samples was sufficient for the thermal steady state for a significant portion of the 1-s exposure. As expected, the 20-s exposures appeared to reach thermal steady state within 1-2 s, but as shown in Fig. 5(e), temperatures drifted higher over the majority of the 20-s thermal profiles. Although the 20-s exposures were expected to represent isothermal reactions, a drift in laser power starting at about 2.5 s caused the moderate increase of about 10% of each peak $\Delta T (\Delta T_p)$ during the final 17.5 s [Fig. 5(e)]. In constant power mode, the laser output had a large power spike as the internal shutter opened, necessitating the use of the constant current mode. Unfortunately, being in the constant current mode caused the power drift seen most noticeably in the longer exposures.

Table 1 shows that, except for the 20-s exposure at 40°C, within each $\tau$ group, there were no statistically significant differences in threshold peak temperature values. This was less clear from Fig. 5 because one must add $T_{amb}$ to the $\Delta T$ values to calculate threshold peak temperature values. Combined, the results from Table 1 and Fig. 5 show that threshold peak temperature was a primary determining factor for damage within each exposure duration. The effect of varying ambient temperature was that it determined the $\Delta T$ required for achieving the damage threshold peak temperature value. This result appeared to be a form of reciprocity between threshold $\Delta T$ at $\tau$ ($\Delta T_p$) and the ambient temperature. When plotted as $\Delta T_p$ versus $T_{amb}$, slopes of $-1.01$, $-0.89$, $-0.96$, and $-0.60$ were obtained for $\tau$ values of 0.05, 0.25, 1.0, and 20 s, respectively (data not shown). Except for the 20-s data, which were skewed by the inexplicably high threshold peak temperature at 40°C ambient, the current results follow a trend expected for reciprocity (i.e., a slope near 1).

**Table 1** Exposure parameters and thermal data for nonpigmented and pigmented cells exposed to laser irradiation.

| Exposure Duration (s) | Wavelength (nm) | MPs/cell | Exposures (n) | Ambient Temperature (°C) | Temperature SD | Boundary of cell death RoI Pixels (n) | Peak temperature (°C) | SD | SEM |
|---|---|---|---|---|---|---|---|---|---|
| 1.0 | 532 | 100 | 8 | 34.7 | 0.4 | 661 | 52.4 | 0.8 | 0.3 |
| | 532 | 200 | 13 | 34.2 | 0.4 | 794 | 51.9 | 0.7 | 0.2 |
| | 532 | 400 | 16 | 34.7 | 0.3 | 1223 | 52.2 | 0.8 | 0.2 |
| | 532 | 800 | 14 | 34.0 | 0.2 | 1369 | 52.5 | 0.9 | 0.2 |
| 3.0 | 532 | 100 | 12 | 34.2 | 0.3 | 894 | 50.4 | 0.8 | 0.2 |
| | 532 | 200 | 9 | 34.0 | 0.2 | 640 | 50.2 | 0.7 | 0.2 |
| | 532 | 400 | 11 | 34.0 | 0.2 | 1050 | 50.2 | 0.4 | 0.1 |
| | 532 | 800 | 8 | 34.0 | 0.1 | 989 | 50.5 | 0.7 | 0.3 |
| 0.05 | 2000 | 0 | 18 | 20.1 | 0.2 | 2017 | 62.2 | 5.2 | 1.2 |
| | 2000 | 0 | 16 | 24.7 | 0.2 | 3207 | 62.5 | 2.0 | 0.5 |
| | 2000 | 0 | 20 | 29.6 | 0.3 | 2049 | 60.1 | 1.3 | 0.3 |
| | 2000 | 0 | 16 | 39.9 | 0.2 | 2003 | 62.3 | 1.3 | 0.3 |
| 0.25 | 2000 | 0 | 15 | 20.0 | 0.1 | 1733 | 59.0 | 1.2 | 0.3 |
| | 2000 | 0 | 12 | 24.7 | 0.2 | 1438 | 59.6 | 1.5 | 0.4 |
| | 2000 | 0 | 13 | 29.6 | 0.3 | 1511 | 59.5 | 2.9 | 0.8 |
| | 2000 | 0 | 12 | 40.1 | 0.3 | 1486 | 61.2 | 1.9 | 0.6 |
| 1.0 | 2000 | 0 | 15 | 20.4 | 0.3 | 2105 | 55.5 | 1.4 | 0.4 |
| | 2000 | 0 | 15 | 25.0 | 0.5 | 1617 | 56.5 | 1.1 | 0.4 |
| | 2000 | 0 | 16 | 29.7 | 0.5 | 1408 | 54.9 | 1.8 | 0.6 |
| | 2000 | 0 | 12 | 39.9 | 0.2 | 1100 | 56.6 | 1.4 | 0.6 |
| 20.0 | 2000 | 0 | 13 | 20.1 | 0.2 | 2907 | 48.3 | 2.6 | 0.8 |
| | 2000 | 0 | 15 | 24.7 | 0.1 | 1944 | 49.2 | 1.5 | 0.5 |
| | 2000 | 0 | 15 | 29.4 | 0.2 | 1841 | 50.2 | 1.2 | 0.4 |
| | 2000 | 0 | 12 | 39.9 | 0.2 | 1390 | 56.1 | 1.5 | 0.5 |

This result corroborates a previous assessment of the effect of pre-exposure fundus temperature ($T_{amb}$) on threshold $\Delta T$ in pigmented rabbit retinas exposed at 488-nm for 10 s.[56] Here, the authors used microthermocouples[41] to determine threshold $\Delta T_p$ in the intact globe, plotted the thresholds (along with some extrapolated thresholds) versus their corresponding pre-exposure fundus temperatures (30°C–44°C), and found a slope of −1.15. This slope indicated reciprocity between threshold $\Delta T$ and pre-exposure fundus temperature. The way these animal studies were set up, the ambient temperature was established for much longer than in our in vitro experiment. Also, of interest, the extrapolated line for the rabbit study crossed the abscissa at 52.4°C, to which the authors attribute the threshold temperature

for damaging the fundus without laser exposure. Notice that this 52.4°C in vivo threshold value for 10 s falls between the in vitro peak temperature thresholds (boundary) for 1 and 20 s in Table 1.

An important implication of our results is that short intervals of nonoptimum pre-exposure temperature did little to affect the required threshold peak temperature to cause photothermal damage in the cultured cells. The 40°C (104°F) ambient temperature condition did not appear to contribute to the damage rate process, as dictated by peak temperature. Likewise, a short time at the ambient temperature of 20°C (68°F) did not increase the peak temperature requirement for damage at the boundary of cell death. Perhaps, for a more sensitive damage rate process
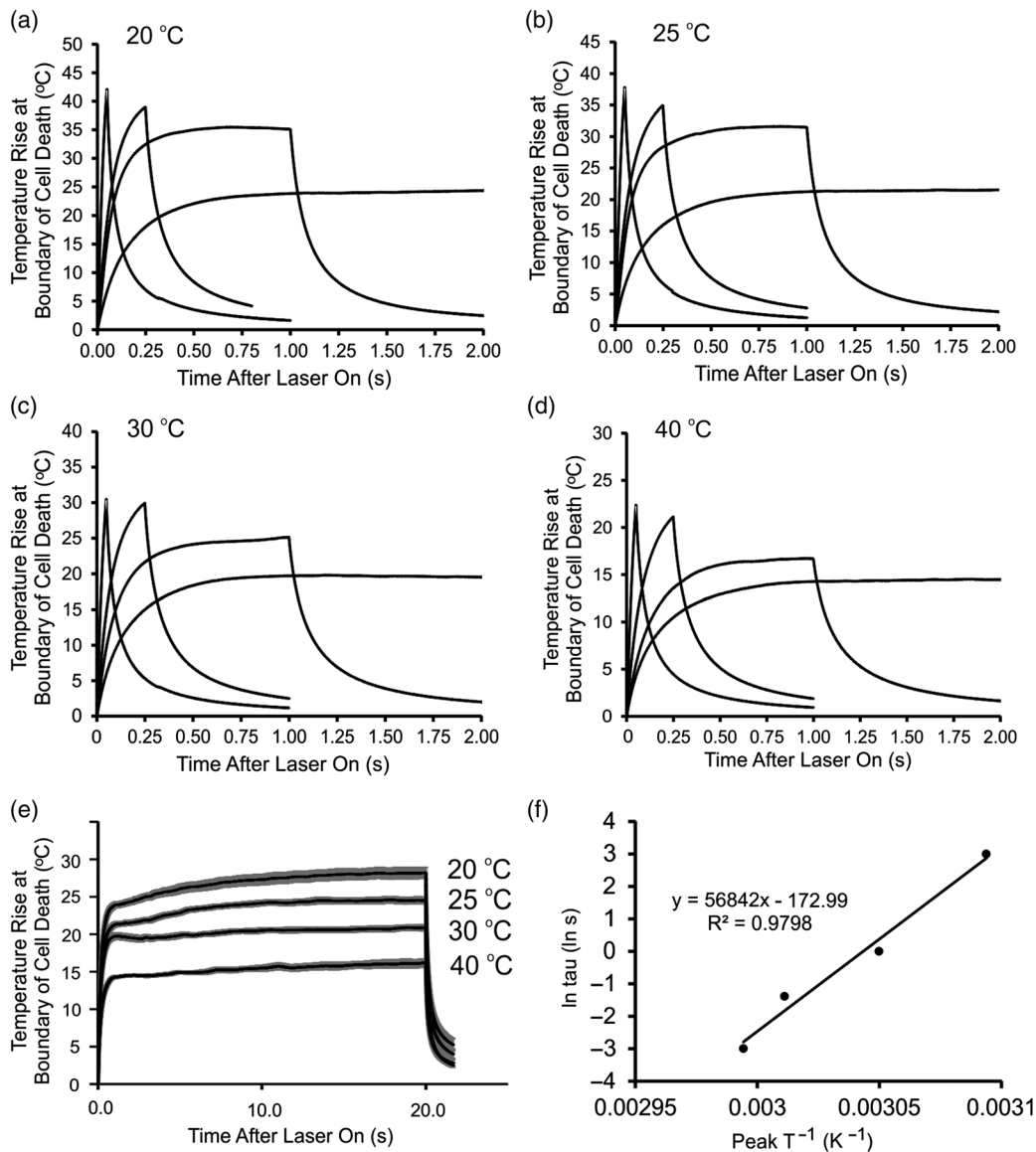
**Fig. 5** Threshold thermal profiles and $A/E_a$ determination for nonpigmented RPE cells exposed at 2 $\mu$m. Initial 2 s of thermal responses to 2-$\mu$m laser exposure at (a) 20°C, (b) 25°C, (c) 30°C, and (d) 40°C. Panel (e) provides full thermal profiles for the duration of the 20-s exposures at each of the four ambient temperatures. All thermal profiles shown in panels (a)–(e) are the mean values at each time point taken from the boundaries of cell death across a wide range of laser irradiances and damage sizes. Panel (f) provides the determination of Arrhenius parameters $A/E_a$ using average threshold $T_p$ values (abscissa) at the four laser exposure durations (ordinate). The values of $A$ and $E_a$ are taken from the $y$-intercept and slope of the resulting line, respectively.

(e.g., apoptosis), the 40°C or 20°C ambient temperature would influence the required threshold peak temperature.

The current study also points to scenarios in which laboratories, without the luxury of owning expensive thermal cameras, or the means of controlling environmental parameters, can perform photothermal damage experiments on cultured cells. Point detection of threshold peak temperature rise in the center of exposed sites can provide thermal data for minimum lesions or as a starting point for computationally building spatial temperature maps that can be overlaid later with damage images.[46] Decoupling laser dose from damage by measuring temperature and minimizing the time that cultures spend at room temperature are primary considerations for improving the quality of the data. A recent article[57] reports the feasibility of using real-time

optoacoustic temperature measurements combined with a non-fluorescent spatially resolved assay for functional mitochondria after 10-s exposure to a thulium laser at 1.94 $\mu$m. Although refinements to the method could aid in both temperature measurement and special resolution of damage assessment, the approach shows potential for assessing photothermal damage processes without the use of a thermal camera.

### 4.1.2 Arrhenius model

*Determining Arrhenius A and $E_a$ values.* The damage integral [Eq. (2)] has been an instrumental tool for evaluating the kinetics of laser-induced damage processes for decades,[7,31,41,42] and we used it to identify an empirical $A/E_a$ pair.

Assuming a constant peak temperature throughout the exposure duration [Eq. (5)], obtaining a conservative estimate of the Arrhenius $A/E_a$ parameters for modeling damage relies on peak temperature values over a range of laser exposure durations. The similar threshold peak temperature values within exposure duration groups (Table 1) indicated that ambient temperature should not affect the values for Arrhenius $A/E_a$ pairs. Considering the similar threshold $T_p$ values within each $\tau$ group, the average threshold peak temperature values were used in the modified Arrhenius plot shown in Fig. 5(f). The $A$ ($1.34 \times 10^{75}$ s$^{-1}$) and $E_a$ ($4.73 \times 10^5$ J mol$^{-1}$) values generated from the straight line in Fig. 5(f) yielded a $T_{crit}$ [Eq. (8)] of 55.6°C (shown in the average ambient temperature row in Table 2). Using these $A/E_a$ values, Eqs. (6) and (7) produced a frequency factor value of $1.12 \times 10^{74}$ s$^{-1}$ and an energy of activation value of $4.74 \times 10^5$ J mol$^{-1}$. Thus, our Arrhenius $A/E_a$ values are in agreement with values reported in the literature. It also indicated that our cell cultures follow the classical photothermal damage rate processes that are apparently inherent to proteins, viruses, bacteria, mammalian cells in culture, tissues, and organs.[30,31,58-60]

Additionally, when we determined $A/E_a$ pairs for the four ambient temperatures within each exposure duration, even though they were not statistically different, an interesting trend appeared (Table 2). As the ambient temperature increased, so did the values for the $A/E_a$ pairs. Indeed, the results in Table 2 show an odd disparity between the relatively similar threshold $T_p$ values across the ambient temperature groups (Table 1), and the large range of calculated values for $A/E_a$ pairs (Table 2) derived using the modified Arrhenius plot [Eq. (5)]. The difference of 40 orders of magnitude for the frequency factor seems remarkably wide, but the corresponding values for the energy of activation increased as well. As suggested by Eq. (8), and the description that followed (Sec. 2.1), $T_{crit}$ can be used as an indicator of the degree of thermal damage. The similar values for critical temperatures in Table 2 would indicate that the $A/E_a$ pairs experimentally determined for each of the ambient temperatures have significance, even though the threshold peak temperature values (Table 1) are essentially the same. We interpret this to mean that the photothermal damage rate process in our cells under the conditions described is the same, regardless of the ambient temperature. It is obvious that the energy requirement to achieve the threshold peak temperature is dependent upon

ambient temperature and that the Arrhenius model appears to be sensitive to this aspect as well.

The 40°C ambient temperature $A/E_a$ pair and critical temperature are strikingly similar to the values obtained by Welch and Polhamus[41] for the nonhuman primate retina ($3.1 \times 10^{99}$ s$^{-1}$, $6.28 \times 10^5$ J mol$^{-1}$, and 57.6°C), even though there were dramatic differences between the *in vitro* and *in vivo* tissues. Referring to the table within the Pearce and Thomsen[41] chapter, there is little similarity between $A/E_a$ pair values across a broad range of sample types, exposure conditions, and methods identifying photothermal damage endpoints, so any similarities between *in vitro* and animal data are likely coincidental.

Conceptually, the results of Table 2 are difficult to reconcile. The slight differences in the slopes and *y*-intercepts for the modified Arrhenius plots for each ambient temperature group obviously led to a wide range of $A/E_a$ values and each $A/E_a$ pair confirmed to the thermodynamically favorably ratio described above. This is a good example of the apparent well-behaved ratio of $A/E_a$ values described by Wright.[60] As described by Wright, the need for the temperature to be in the Kelvin scale may produce an artifact when the range of temperatures involved in biological processes is relatively narrow. In our dataset to determine $A/E_a$ values, the difference between threshold peak temperature values for the 0.05- and 20-s exposures was only about 12 K (50°C–62°C), which corresponds to about 4% (323.15 and 335.15 K). Likewise, the values on the abscissa in Fig. 5(f) clearly show this narrow range.

Regardless of nuances described above and how appealing it may be to depict differences in $A/E_a$ at the different ambient temperature conditions, these data indicate no significant differences in threshold peak temperatures within each exposure duration group. This conclusion also supports the assumptions that the damage rate process within each $\tau$ group is peak temperature dependent and ambient temperature independent, and that the biochemical response of the cells to laser exposure was unaltered by the short intervals of temperature outside the optimum. With this assessment, the four threshold peak temperatures within each exposure duration group were considered replicates, and the use of the average $A/E_a$ pair is appropriate.

In an effort to determine how well the average $A/E_a$ pair predicts damage in our cell culture system, we solved for the damage integral at each temperature-time point of the averaged empirical thermal profiles and identified the $\Omega$ value at the end of the exposure time ($\Omega$ at $\tau$). Recall that we set $\Omega = 1$ in Eq. (4)

**Table 2** Empirically determined energy of activation ($E_a$), frequency factor ($A$), and critical temperature values for hTERT-RPE1 cells exposed to laser irradiation at 2 $\mu$m or 532 nm at various ambient temperatures. Analysis was as per Eq. (5) and Fig. 5(f). Cells exposed at 2 $\mu$m and 532 nm were nonpigmented and pigmented, respectively.

| Ambient temperature (°C) | Arrhenius $E_a$ (J mol$^{-1}$) | | Arrhenius $A$ (s) | | Critical temperature (°C) | |
|---|---|---|---|---|---|---|
| | 2 $\mu$m | 532 nm | 2 $\mu$m | 532 nm | 2 $\mu$m | 532 nm |
| Ave | 473,000 | | $1.34 \times 10^{75}$ | | 55.6 | |
| 20 | 383,000 | | $1.18 \times 10^{61}$ | | 54.5 | |
| 25 | 395,000 | | $6.05 \times 10^{62}$ | | 55.3 | |
| 30 | 477,000 | | $1.29 \times 10^{78}$ | | 54.6 | |
| 35 | | 482,000 | | $1.98 \times 10^{77}$ | | 53.0 |
| 40 | 636,000 | | $3.16 \times 10^{100}$ | | 57.8 | |

**Table 3** Arrhenius integral ($\Omega$) at the end of laser exposure solved from threshold thermal profiles. Using the average (Ave) or individual (Opt) $A/E_a$ values in Table 2, the $\Omega$ value was calculated at each time point of the respective empirical thermal profiles [Figs. 5(a)–5(e)]. Data represent the $\Omega$ value at the end of the laser exposure.

| Ambient temperature (°C) | $\Omega$ value (Ave $E_a/A$) | | | | $\Omega$ value (Opt $E_a/A$) | | | |
|---|---|---|---|---|---|---|---|---|
| | 0.05 s | 0.25 s | 1.0 s | 20.0 s | 0.05 s | 0.25 s | 1.0 s | 20.0 s |
| 20 | 0.11 | 0.25 | 0.57 | 0.21 | 0.12 | 0.37 | 1.04 | 0.84 |
| 25 | 0.15 | 0.35 | 0.75 | 0.41 | 0.11 | 0.32 | 0.83 | 0.84 |
| 30 | 0.05 | 0.39 | 0.26 | 0.79 | 0.10 | 0.88 | 0.56 | 1.71 |
| 40 | 0.21 | 1.07 | 0.83 | 15.50 | 0.16 | 0.71 | 0.26 | 4.44 |

by virtue of the thermal profiles being threshold data at the boundary of cell death. Unfortunately, no average thermal profile exists that represents the mean threshold peak temperature across the four ambient temperatures within each exposure duration because the $\Delta T$ profiles differ. Therefore, we used the average $A/E_a$ pair to determine "$\Omega$ at $\tau$" values for each of the 16 mean thermal profiles represented in Fig. 5, converting temperature units to K. Without an analytical solution to the thermal profiles, which had a temporal resolution of 1.25 ms, we performed a summation of Arrhenius equations at each time step during the mean thermal profiles, with correction by Simpson's rule for numerical integration. The corresponding $\Omega$ values at $\tau$ are given in Table 3. A few of the $\Omega$ values at $\tau$ were near the value of 1. Table 3 also shows that the $\Omega$ at $\tau$ values computed using the optimized $A/E_a$ values within each ambient temperature group were only slightly better than those from the average $A/E_a$ pair.

Overall, Table 3 indicates that for the majority of cases, the $A/E_a$ pairs from the modified Arrhenius plot method underestimated damage ($\Omega = 1$) in the laser-exposed cells. This could be important for modeling efforts to predict photothermal damage using Eq. (5). To quantify the significance of these variances, we calculated the factor by which each time point in the thermal profiles needed to be scaled in order to bring the damage integral values at $\tau$ to a value of 1 [Eq. (9)]. These scaling factors (SFs) provide a quantifiable measure for the potential error of the entire thermal profile. As the corrections take place early in the exposure, the change in temperatures of the new thermal profile builds on the new trend (up or down):

$$T_{new} = ((T_{orig} \times SF) - T_{orig}) + T_{orig}. \tag{9}$$

Table 4 shows that little scaling was needed to force each of the 16 threshold thermal profiles to satisfy $\Omega = 1$ at $\tau$. The only thermal profiles >6% scaling were three of the 0.05-s profiles, and the 20-s profile at 40°C. This observation indicated that all of our empirical threshold thermal profiles were within 10% of their ideal using the averaged $A/E_a$ values. With all the steps involved in obtaining thermal profiles at the boundary for the dozens of laser exposures, the accuracy of the thermal camera, and the nuances associated with obtaining the $A/E_a$ pair, the 10% or less scaling needed to bring the thermal profiles into alignment would seem an excellent result.

Using the SFs, the scaled threshold peak temperature values eliminated all effects of ambient temperature (Table 4), especially the 20-s data. The deviation (STDEV ÷ Ave) of scaled threshold peak temperature values within exposure duration groups was 0.4%–0.6%. The deviations for the empirical threshold $T_p$ values were 1.5%–1.8%, except for the 20-s data that was 6.9%. As expected for correction to the Arrhenius law, the resulting scaled $\Delta T_p$ values provide a clear signal for reciprocity. Plotting the corrected $\Delta T_p$ values versus ambient temperature (data not shown) produced straight lines for all four exposure duration groups, with each slope near $-1.0$, and $y$-intercepts close to each Arrhenius $T_p$ value (67.9°C, 63.0°C, 56.0°C, and 51.3°C for 0.05, 0.25, 1.0, and 20 s, respectively). This analysis helped to quantify the often-used observation that threshold peak temperature values increase as exposure duration is shortened.

**Table 4** Threshold peak temperature values ($T_p$) empirically determined (Emp $T_p$) or scaled (scaled $T_p$) by Eq. (9) SF, such that "$\Omega = 1$ at $\tau$" using the "Ave" $A/E_a$ pair shown in Table 2. Percent variance is built into the SF values.

| Ambient temperature (°C) | 0.05 s | | | 0.25 s | | | 1.0 s | | | 20.0 s | | |
|---|---|---|---|---|---|---|---|---|---|---|---|---|
| | Emp $T_p$ (°C) | SF | Scaled $T_p$ (°C) | Emp $T_p$ (°C) | SF | Scaled $T_p$ (°C) | Emp $T_p$ (°C) | SF | Scaled $T_p$ | Emp $T_p$ | SF | Scaled $T_p$ (°C) |
| 20 | 62.2 | 1.072 | 66.6 | 59.0 | 1.046 | 61.8 | 55.5 | 1.020 | 56.5 | 48.3 | 1.060 | 51.3 |
| 25 | 62.5 | 1.061 | 66.4 | 59.6 | 1.035 | 61.8 | 56.5 | 1.010 | 56.8 | 49.2 | 1.034 | 51.0 |
| 30 | 60.1 | 1.103 | 66.3 | 59.5 | 1.032 | 61.6 | 54.9 | 1.048 | 57.3 | 50.2 | 1.009 | 50.9 |
| 40 | 62.3 | 1.051 | 65.7 | 61.2 | 0.998 | 61.3 | 56.6 | 1.006 | 57.0 | 56.1 | 0.908 | 51.0 |

## 4.2 Effects of Pigmentation on Threshold Temperature

Taking advantage of our ability to alter the amount of intracellular pigmentation in the hTERT-RPE1 cells, we investigated whether MPs undergo a chemical reaction during photothermal heating that effects the damage rate process. Although our method could not distinguish whether a proposed photochemical byproduct of photothermal exposure[27,28] was the result of photon absorption directly (photochemical) or the temperature rise due to photon absorption (photothermal), it was designed to determine if any alteration in threshold damage rate does occur.

Table 1 provides $T_{amb}$ and threshold $T_p$ values for 1- and 3-s exposures of RPE cells containing up to an eightfold difference in the number of melanosomes offered cells in culture the day prior to exposure. Note the well-controlled ambient temperature across all 91 exposures (34.3°C ± 0.3°C) at 532 nm. Peak temperatures at the boundary of cell death were essentially identical within the two exposure duration groups. The thermal profiles within each exposure duration were strikingly similar, and Fig. 6 provides a plot with each average thermal profile for pigmentation of 100, 200, 400, and 800 MPs/cell. Although the threshold peak temperature values were the same (Table 1), Fig. 6 clearly shows a change in the shape of the two thermal profiles resulting from exposure to cells having 800 MPs/cell. At the lower pigmentation levels, there was no pigment-dependent effect. In fact, due to the overall similarities in thermal profiles, the data actually indicate a high level of precision for extracting thermal data from the many boundary RoIs.

Clearly, the various levels of pigmentation dictated different laser irradiances to generate damage. Additionally, for the threshold $T_p$ characterizations, only those exposures resulting in damage were included. In general, laser irradiances of $60 - 260$ W cm$^{-2}$ (1 s) and $45 - 300$ W cm$^{-2}$ (3 s) generated damage for boundary analysis across the range of pigmentation. By expanding the range of laser irradiances lower, negative damage results were recorded and used in the Probit software to estimate threshold ED$_{50}$ values. Table 5 provides Probit data for the exposure durations and pigmentation levels shown in Table 1

and Fig. 6, plus a 50 and 300 MPs/cell scenario for 3-s exposures.

As expected, the higher pigmentation, which effectively increases the absorption coefficient ($\mu_a$), required less laser irradiance to cause damage, as evidenced by the ED$_{50}$ values in Table 5. The 95% FLs were within 10% of their respective ED$_{50}$ values, except for the 400 and 800 MPs/cell data for 1-s exposures (11% and 24%, respectively). The large values of Probit slopes (Table 5), representing the first derivative at a 50% probability, indicate robust data.

The *in vitro* ED$_{50}$ values did not track linearly with absorption coefficient ($\mu_a$), represented by the amount of intracellular pigmentation. As dictated by the heat-diffusion equation, a laser exposure much reach thermal steady-state in order for laser irradiance to correlate linearly with temperature rise. Referring to Fig. 6, the 3-s exposure was approaching steady state, so the data were plotted in Fig. 7. From the graph, both the 1- and 3-s data had power curve with negative exponents of less than 0.7, compared to the idealized case ($\mu_a^{-1}$). The figure indicates a complex dependence upon both exposure duration and pigment. These trends were derived from samples having the same sample boundary conditions (bottom to top; air, glass, cells, the same volume of buffer, air), so they are comparable. The *in vitro* sample boundaries differ from the tissue boundaries in the eye, and we would not expect the same ED$_{50}$ values, but the trends shown here could translate to retinal or pigmented skin ED$_{50}$ studies. Clearly, an advantage lies in characterizing damage rate mechanisms using threshold peak temperatures, where the key determinant is laser exposure duration.

Although we had only two threshold temperature values (1 and 3 s) to plot as Eq. (5) (data not shown), we obtained the $A/E_a$ values reported in Table 2. These values fit the ambient temperature trend described above for the 2-$\mu$m data, falling between the $A/E_a$ values for ambient temperatures of 30°C and 40°C without pigment. We applied the same scaling method to these two empirical threshold thermal profiles and found that they were farther from the Arrhenius ideal values than most of the nonpigmented profiles. The 1- and 3-s thermal data required a 16% (SF 1.160) and 10% (SF 1.100) increase at each integration time point to achieve $\Omega = 1$, respectively, which is also remarkable overall.

## 4.3 Comparisons across Experimental Parameters

Comparing data within the nonpigmented and pigmented sets was straightforward because the laser parameters and the layers making up samples were the same. However, there were a few salient points for comparison between the nonpigmented and pigmented data. Both had a 1-s exposure. The threshold peak temperature values for these 1-s exposures differed by about 3.6°C, with the bulk water heating at 2 $\mu$m being the higher value. One explanation for this is that because the pixels of the thermal camera were ~8 $\mu$m × 8 $\mu$m, it was unable to capture the expected higher temperature rise near the surface of the absorbing 1 $\mu$m × 1 $\mu$m MP. Thus, the bulk water was being heated equally across the pixel area by the 2-$\mu$m laser, but the heating around the tiny MP had diffused significantly to fill the area of the single pixel of the thermal camera. However, at the highest level of pigmentation (800 MPs/cell), where clumping of MPs was most common, the shape of the thermal profile was different (Fig. 6) even though the threshold peak temperature value was no greater than that generated by the lowest level of pigmentation.
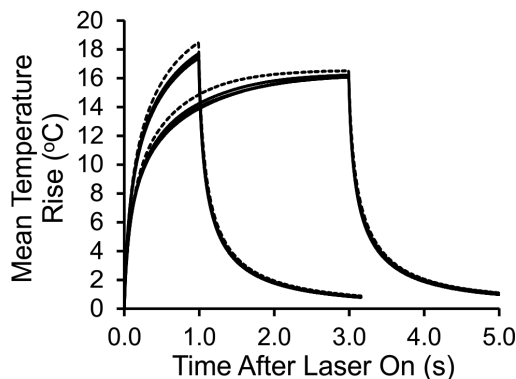


**Fig. 6** Threshold thermal profiles for pigmented RPE cells exposed at 532 nm. Lines represent mean temperature history for thermal camera pixels at the boundary of cell death for 1- and 3-s exposures with each level of pigmentation. Pigmentation levels correspond to normal cellular uptake of MPs when provided at 100, 200, 400, and 800 MPs/cell on the previous day. Dashed lines correspond to data for 800 MPs/cell. Data incorporate laser irradiances of 60–260 W cm$^{-2}$ (1 s) and 45–300 W cm$^{-2}$ (3 s) to show irradiance independence at the boundaries of cell death.

**Table 5** Threshold $ED_{50}$ irradiance values for pigmented cells exposed at 532 nm. Probit[54,55] analysis was performed on binary yes/no damage data. Upper FL (UFL) and lower FL (LFL) provide 95% confidence intervals, and slope of the Probit curve at 50% probability (Probit slope). Note that none of the LFL and UFL overlap with those of neighboring thresholds.

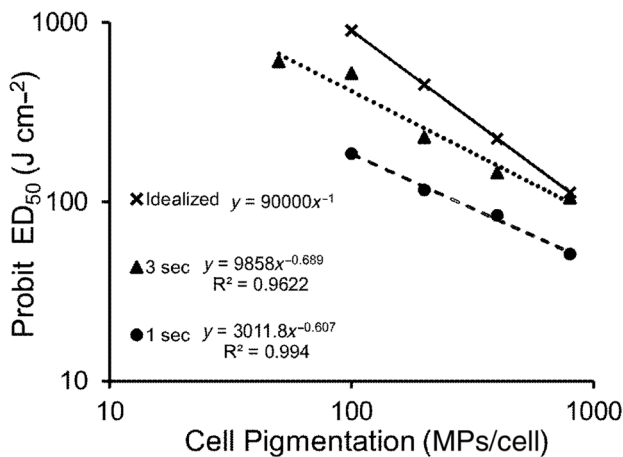| Exposure duration (s) | Wavelength (nm) | MPs/cell | $ED_{50}$ value (W cm$^{-2}$) | LFL (W cm$^{-2}$) | UFL (W cm$^{-2}$) | Probit slope |
|---|---|---|---|---|---|---|
| 1.0 | 532 | 100 | 186.0 | 172.0 | 198.0 | 16.4 |
| | 532 | 200 | 116.0 | 109.0 | 122.0 | 18.9 |
| | 532 | 400 | 83.9 | 72.3 | 93.2 | 9.3 |
| | 532 | 800 | 51.0 | 46.3 | 55.7 | 29.6 |
| 3.0 | 532 | 50 | 202.0 | 188.0 | 216.0 | 13.1 |
| | 532 | 100 | 174.0 | 165.0 | 181.0 | 30.2 |
| | 532 | 200 | 76.2 | 68.6 | 83.2 | 16.0 |
| | 532 | 300 | 61.2 | 56.3 | 65.8 | 21.6 |
| | 532 | 400 | 48.4 | 42.9 | 53.2 | 15.5 |
| | 532 | 800 | 35.2 | 26.7 | 41.4 | 13.8 |



**Fig. 7** Threshold $ED_{50}$ radiant exposure values (J cm$^{-2}$) versus pigmentation for cells exposed at 532 nm. Data for 1-s (dashed line) and 3-s (dotted line) exposures are compared to the idealized condition (solid line) in which threshold laser damage is reciprocally related to cell pigmentation ($x^{-1}$).

Additionally, Table 2 includes the $A/E_a$ values for the pigmented data at an ambient temperature of 35°C. Understandably, the data are unreliable due to having only two data points, but the values estimated for $A/E_a$ fall into the expected trend (between 30°C and 40°C values for nonpigmented exposures). Also of note is how close the 1-s 35°C threshold peak temperature values (average of 52.3°C) is near the $T_{crit}$ value (Table 2), as per expected from Eq. (5).

## 5 Summary

Adopting the concept that the spatial boundary between live and dead cells postlaser exposure is equivalent to a minimum visible lesion provided an opportunity to compare thermal responses generated by disparate laser and sample properties. The extracted thermal profiles and threshold peak temperature values

from damage boundaries (threshold $T_p$) were very similar within each laser exposure duration, regardless of laser irradiance, ambient temperature, or the size of the affected region. The wide range of laser exposure durations (0.05–20 s), ambient temperatures, and effective absorption coefficients ($\mu_a$) used in this study better demonstrated photothermal damage rate processes than our previous study.[47]

Comparing the $ED_{50}$ threshold analysis with that of the threshold $T_p$ values across multiple levels of intracellular pigmentation underscored the significance of decoupling laser irradiance and threshold $ED_{50}$ values. There are nearly always varying optical and thermal properties within a biological sample, which leads to varied temperature rises that ultimately dictate the damage rate processes. As expected, we found that the complex combination between pigmentation ($\mu_a$), diffusivity, and thermal properties of the sample led to threshold $ED_{50}$ irradiances that generated the $\tau$-specific threshold thermal response required to generate damage for 1 and 3-s exposures (Table 5 and Fig. 6).

It was unclear whether peak temperature alone, or the rate of achieving that peak temperature, is the determinant for cell death. This important distinction, discussed below regarding the damage integral, can be assessed because each threshold thermal profile is defined as satisfying $\Omega = 1$. Varying the ambient temperature during laser exposure was meant to distinguish whether peak temperature or the acceleration of temperature rise is key to the rate process. Our results support the need to achieve a specific ($\tau$-dependent) peak temperature for cell death. The small SDs in Fig. 5 suggest that, regardless of how peak temperature was achieved (changing ambient temperature), the temperature rise needed for damage follows the reciprocal trend of exposure duration ($\tau^{-1}$) within each ambient temperature. This result also indicates that the short time cells spent at the various ambient temperatures prior/during laser exposure in our experiments did not change downstream biological processes that lead to death as assessed here.

To characterize mathematically the photothermal damage rate processes for the current cell culture model, we determined

the Arrhenius rate parameters, $A/E_a$, using just the step function of threshold $T_p$ versus $\tau$ [Fig. 5(f)] as derived in Eq. (5). We found that the $A/E_a$ values varied depending upon ambient temperature (Table 2), even though there were no significant differences in threshold peak temperature for each exposure duration (Table 1). Neither these ambient temperature-specific $A/E_a$ values nor the average $A/E_a$ values across the entire dataset solved for a damage integral of 1 when integrating the individual thermal profiles. However, because the damage integral is so temperature dependent, only minor corrections (0.6%–10.3%) to temperatures at each time point in the empirical thermal profiles were needed to make them all conform to $\Omega = 1$. Thus, we conclude that our empirical data were all within 10% of the ideal Arrhenius rate law for photothermal damage rate processes.

In conclusion, our scaled empirically derived frequency factor and energy of activation pair ($A/E_a$) resulted in a value of unity for the damage integral for all 16 combinations of ambient temperature and exposure duration. This outcome supports the hypothesis that cells at the boundary of cell death are equivalent to a minimum visible lesion. The 10% or less scaling of temperature required to achieve this unanimity of the condition, "$\Omega = 1$ at $\tau$" is remarkable considering the multiple steps involved in determining threshold thermal profiles. This precision of the kinetic approach signifies a strong validation for the use of the damage integral. The overall fidelity of the method is a tribute to the reproducibility of the *in vitro* model and the methods used to determine boundary regions of interest. Finally, it is clear that our RPE cells have fast and accurate "thermostats" that trigger metabolic pathways for damage. We look forward to using our method to identify potential differences in threshold temperature history for damage in other cell types and tissues while searching for specific macromolecules responsible for the metabolic triggers associated with photothermal damage rate processes.

## Disclosures

The authors have no relevant financial interests in this article and no potential conflicts of interest to disclose.

## Acknowledgments

## References

1. W. Lilienblum et al., "Alternative methods to safety studies in experimental animals: role in the risk assessment of chemicals under the new European Chemicals Legislation (REACH)," *Arch. Toxicol.* **82**(4), 211–236 (2008).
2. A. H. Piersma et al., "A critical appraisal of the process of regulatory implementation of novel in vivo and in vitro methods for chemical hazard and risk assessment," *Crit. Rev. Toxicol.* **44**(10), 876–894 (2014).
3. S. Gordon et al., "Non-animal models of epithelial barriers (skin, intestine and lung) in research, industrial applications and regulatory toxicology," *ALTEX* **32**(4), 327–378 (2015).
4. C. D. Clark, III, W. J. Marshall, and R. J. Thomas, "Theoretical analysis of multiple-pulse thermal damage thresholds of the retina," *J. Laser Appl.* **25**(1), 012005 (2013).
5. E. M. Ahmed et al., "Maxwell's equations-based dynamic laser-tissue interaction model," *Comput. Biol. Med.* **43**(12), 2278–2286 (2013).
6. K. Schulmeister et al., "Ex vivo and computer model study on retinal thermal laser-induced damage in the visible wavelength range," *J. Biomed. Opt.* **13**(5), 054038 (2008).
7. J. Mathieu and K. Schulmeister, "Validation of a computer model to predict laser induced retinal injury thresholds," *J. Laser Appl.* **29**, 032004 (2017).
8. M. L. Denton et al., "In vitro model that approximates retinal damage threshold trends," *J. Biomed. Opt.* **13**(4), 054014 (2008).
9. M. L. Denton et al., "Damage thresholds for cultured retinal pigment epithelial cells exposed to lasers at 532 nm and 458 nm," *J. Biomed. Opt.* **12**(3), 034030 (2007).
10. M. L. Denton et al., "Damage thresholds for exposure to NIR and blue lasers in an in vitro RPE cell system," *Invest. Ophthalmol. Visual Sci.* **47**, 3065–3073 (2006).
11. D. W. Bäuerie, "Thermal, photophysical, and photochemical processes," Chapter 2 in *Laser Processing and Chemistry*, D. Bäuerle, Ed., pp. 13–38, 4th ed., Springer-Verlag, Berlin, Heidelberg (2011).
12. T. Finkel, "The metabolic regulation of aging," *Nat. Med.* **21**(12), 1416–1423 (2015).
13. J. L. R. Roti, "Cellular responses to hyperthermia (40–46°C): cell killing and molecular events," *Int. J. Hyperthermia* **24**(1), 3–15 (2008).
14. I. B. Slimen et al., "Reactive oxygen species, heat stress and oxidative-induced mitochondrial damage. A review," *Int. J. Hyperthermia* **30**(7), 513–523 (2014).
15. B. Szczesny et al., "Time-dependent and organ-specific changes in mitochondrial function, mitochondrial DNA integrity, oxidative stress and mononuclear cell infiltration in a mouse model of burn injury," *PLoS One* **10**(12), e0143730 (2015).
16. Y. Zhang and S. K. Calderwood, "Autophagy, protein aggregation and hyperthermia: a mini-review," *Int. J. Hyperthermia* **27**(5), 409–414 (2011).
17. F. Despa et al., "The relative thermal stability of tissue macromolecules and cellular structure in burn injury," *Burns* **31**(5), 568–577 (2005).
18. F. C. Henriques, "Studies of thermal injury V. The predictability and significance of thermally induced rate processes leading to irreversible epidermal injury," *Arch. Pathol.* **43**, 489–502 (1947).
19. F. C. Henriques and A. R. Moritz, "Studies of thermal injury: I. The conduction of heat to and through skin and the temperatures attained therein: a theoretical and experimental investigation," *Am. J. Pathol.* **23**, 531–549 (1947).
20. A. R. Moritz and F. C. Henriques, "Studies of thermal injury II. The relative importance of time and surface temperature in the causation of cutaneous burns," *Am. J. Pathol.* **23**, 695–720 (1947).
21. A. R. Moritz, "Studies of thermal injury III. The pathology and pathogenesis of cutaneous burns: an experimental study," *Am. J. Pathol.* **23**, 915–934 (1947).
22. J. R. Lepock, "Protein denaturation in intact hepatocytes and isolated cellular organelles during heat shock," *J. Cell Biol.* **122**(6), 1267–1276 (1993).
23. J. R. Lepock, "Cellular effects of hyperthermia: relevance to the minimum dose for thermal damage," *Int. J. Hyperthermia* **19**(3), 252–266 (2003).
24. J. R. Lepock, "Measurement of protein stability and protein denaturation in cells using differential scanning calorimetry," *Methods* **35**, 117–125 (2005).
25. V. Nikoletopoulou et al., "Crosstalk between apoptosis, necrosis and autophagy," *Biochim. Biophys. Acta* **1833**(12), 3448–3459 (2013).
26. M. L. Goodall et al., "The autophagy machinery controls cell death switching between apoptosis and necroptosis," *Dev. Cell* **37**, 337–349 (2016).
27. B. S. Gerstman and R. D. Glickman, "Activated rate processes and a specific biochemical mechanism for explaining delayed laser induced thermal damage to the retina," *J. Biomed. Opt.* **4**(3), 345–351 (1999).

28. S. J. Till et al., "A new model for laser-induced thermal damage in the retina," *Bull. Math. Biol.* **65**, 731–746 (2003).
29. R. Birngruber, "Thermal modeling in biological tissues," in *Lasers in Biology and Medicine*, F. Hillenkamp, R. Pratesi, and A Sacchi, Eds., p. 77, Plenum Press, New York (1980).
30. X. He and J. C. Bischof, "Quantification of temperature and injury response in thermal therapy and cryosurgery," *Crit. Rev. Biomed. Eng.* **31**(5–6), 355–422 (2003).
31. J. Pearce and S. Thomsen, "Rate process analysis of thermal damage," in *Optical Thermal Response of Laser-Irradiated Tissue*, A. J. Welch and M. J. C. van Germert, Eds., pp. 487–549, 2nd ed., Plenum Press, New York (2011).
32. S. L. Jacques, "Ratio of entropy to enthalpy in thermal transitions in biological tissues," *J. Biomed. Opt.* **11**(4), 041108 (2006).
33. N. T. Wright and J. D. Humphrey, "Denaturation of collagen via heating: an irreversible rate process," *Annu. Rev. Biomed. Eng.* **4**, 109–128 (2002).
34. S. A. Sapareto and W. C. Dewey, "Thermal dose determination in cancer therapy," *Int. J. Radiat. Oncol. Biol. Phys.* **10**(6), 787–800 (1984).
35. P. Wust et al., "Hyperthermia in combined treatment of cancer," *Lancet Oncol.* **3**, 487–497 (2002).
36. W. C. Dewey, "Arrhenius relationships from the molecule and cell to the clinic," *Int. J. Hyperthermia* **10**, 457–483 (1994).
37. M. W. Dewhirst et al., "Basic principles of thermal dosimetry and thermal thresholds for tissue damage from hyperthermia," *Int. J. Hyperthermia* **19**(3), 267–294 (2003).
38. J. T. Beckham et al., "Assessment of cellular response to thermal laser injury through bioluminescence imaging of heat shock protein 70," *Photochem. Photobiol.* **79**, 76–85 (2004).
39. N. A. Moussa, E. N. Tell, and E. G. Cravalho, "Time progression of hemolysis of erythrocyte populations exposed to supraphysiological temperatures," *J. Biomech. Eng.* **101**, 213–217 (1979).
40. N. T. Wright, "On a relationship between the Arrhenius parameters from thermal damage studies," *J. Biomech. Eng.* **125**, 300–304 (2003).
41. A. J. Welch and G. D. Polhamus, "Measurement and prediction of thermal injury in the retina of Rhesus monkey," *IEEE Trans. Biomed. Eng.* **31**, 633–644 (1984).
42. A. N. Takata et al., "Thermal model of laser induced eye damage," Final Report Contract F41609-74-C-0005, USAF School of Aerospace Medicine, Brooks AFB, San Antonio, Texas, IIT Research Institute, Chicago, Illinois (1974).
43. Y. Yang, A. J. Welch, and H. G. Rylander, "Rate process parameters of albumen," *Lasers Surg. Med.* **11**, 188–190 (1991).
44. W. T. Ham, Jr. et al., "The nature of retinal radiation damage: dependence on wavelength, power level, and exposure time," *Vision Res.* **20**, 1105–1111 (1980).
45. W. T. Ham, Jr. et al., "Sensitivity of the retina to radiation damage as a function of wavelength," *Photochem. Photobiol.* **29**, 735–743 (1979).
46. D. M. Simanovskii et al., "Cellular tolerance to pulsed hyperthermia," *Phys. Rev. E* **74**, 011915 (2006).
47. M. L. Denton et al., "Spatially correlated microthermography maps threshold temperature in laser-induced damage," *J. Biomed. Opt.* **20**(7), 079801 (2015).
48. M. L. Denton et al., "Hyperthermia sensitizes pigmented cells to laser damage without changing threshold damage temperature," *J. Biomed. Opt.* **18**(11), 110501 (2013).
49. M. L. Denton et al., "Determination of threshold average temperature for cell death in an in vitro retinal model using thermography," *Proc. SPIE* **7175**, 71750G (2009).
50. A. E. Dontsov, R. D. Glickman, and M. Ostrovsky, "Retinal pigment epithelium pigment granules stimulate the photo-oxidation of unsaturated fatty acids," *Free Radical Biol. Med.* **26**, 1436–1446 (1999).
51. M. L. Denton et al., "Thermal and damage data form multiple microsecond pulse trains at 532 nm in an in vitro retinal model," *Proc. SPIE* **8941**, 89410J (2014).
52. M. L. Denton et al., "Evidence of thermal additivity during short laser pulses in an in vitro retinal model," *Proc. SPIE* **9321**, 93210G (2015).
53. M. L. Denton et al., "Correlating measured transient temperature rises with damage rate processes in cultured cells," *Proc. SPIE* **10062**, 100620I (2017).
54. D. J. Finney, *Probit Analysis*, Cambridge University Press, New York (1971).
55. C. P. Cain, G. D. Noojin, and L. Manning, "A comparison of various probit methods for analyzing yes/no data on a log scale," USAF Technical Report AL/OE-TR-1996-0102, USAF School of Aerospace Medicine, Brooks Air Force Base, San Antonio, Texas (1996).
56. G. D. Polhamus and A. J. Welch, "Effect of pre-exposure fundus temperature on threshold lesion temperatures in the laser-irradiated rabbit retina," *Invest. Ophthalmol. Visual Sci.* **14**, 562–565 (1975).
57. Y. Miura et al., "Real-time optoacoustic temperature determination on cell cultures during heat exposure: a feasibility study," *Int. J. Hyperthermia* **36**, 466–472 (2019).
58. B. Rosenberg et al., "Quantitative evidence for protein denaturation as the cause of thermal death," *Nature* **232**, 471–473 (1971).
59. B. Rosenberg and T. P. Williams, "The thermal decomposition of visual pigments as a compensation law process," *Vision Res.* **11**, 613–615 (1971).
60. N. T. Wright, "On a relationship between the Arrhenius parameters from thermal damage studies," *J. Biomech. Eng.* **125**, 300–304 (2003).

Biographies of the authors are not available.